Momentum transfer in a turbulent, particle-laden Couette flow

David H. Richter and Peter P. Sullivan

Additional information on Phys. Fluids

Momentum transfer in a turbulent, particle-laden Couette flow

David H. Richter and Peter P. Sullivan
National Center for Atmospheric Research, Boulder, Colorado 80307, USA

A point-force model is used to study turbulent momentum transfer in the presence of moderate mass loadings of small (relative to Kolmogorov scales), dense (relative to the carrier phase density) particles. Turbulent Couette flow is simulated via direct numerical simulation, while individual particles are tracked as Lagrangian elements interacting with the carrier phase through a momentum coupling force. This force is computed based on the bulk drag of each particle, computed from its local slip velocity. By inspecting a parameter space consisting of particle Stokes number and mass loading, a general picture of how and under what conditions particles can alter near-wall turbulent flow is developed. In general, it is found that particles which adhere to the requirements for the point-particle approximation attenuate small-scale turbulence levels, as measured by wall-normal and spanwise velocity fluctuations, and decrease turbulent fluxes. Particles tend to weaken near-wall vortical activity, which in turn, through changes in burst/sweep intensities, weakens the ability of the turbulent carrier-phase motion to transfer momentum in the wall-normal direction. Compensating this effect is the often-ignored capacity of the dispersed phase to carry stress, resulting in a total momentum transfer which remains nearly unchanged. The results of this study can be used to interpret physical processes above the ocean surface, where sea spray potentially plays an important role in vertical momentum transfer. © *2013 AIP Publishing LLC*. [http://dx.doi.org/10.1063/1.4804391]

I. INTRODUCTION

The addition of particles to a turbulent flow is a fundamental problem studied extensively in the past using both experiments and numerical simulations. Motivated by a wide range of applications, for example, turbidity currents,[1] spray combustion,[2] or cloud physics,[3] various dispersed phase processes such as particle deposition, particle segregation, and turbulence modification have been investigated in detail. The present study focuses on the ability of the dispersed phase to alter momentum transport in a wall-bounded turbulent flow. This is an important question, for example, in deciding how to treat sea spray in atmospheric models; currently, an ongoing debate exists over whether or not the presence of such a dispersed phase in the near-surface atmospheric boundary layer is dynamically important, and whether it influences the drag of the ocean surface at high winds.[4–7]

Numerous factors control whether or not particles enhance or attenuate turbulence levels in a flow. Based on experimental evidence, Gore and Crowe[8] cite the ratio of the particle diameter to the turbulence integral length scale as determining whether or not turbulence will be enhanced, and Hetsroni[9] uses the particle Reynolds number to distinguish how particles modify turbulence. More recently, Tanaka and Eaton[10] nondimensionalize the governing dispersed phase equations and define a nondimensional parameter which they find separates the results of previous wall-bound experimental studies into regions of turbulence augmentation and attenuation.

Attempts to define a single governing parameter highlight the difficulty associated with predicting the effect of particles on turbulence: the many simultaneous physical effects are difficult to distinguish from one another. For small spheres, it is generally agreed that since the particle Reynolds numbers remain small and their disturbances to the velocity field remain negligible, the

added drag on the carrier phase results in an attenuation of turbulence. As particles increase in size, however, two effects can become important: the particle Reynolds number can increase to the point where particles shed wakes, thereby adding turbulent energy at small scales,[9] and the particle diameter can approach the size of the smallest turbulent eddies. The latter effect has been shown to increase local dissipation up to 10 radii away,[11,12] and is therefore not the same effect as solely increasing the particle Reynolds number. Also, differences in Stokes numbers (the ratio of the particle acceleration time scale to a flow time scale) dictate how efficiently the particles can preferentially concentrate, particularly in near-wall streaks, which affects various statistics due to enhancement of local concentrations.[13–15]

The present study focuses on particles smaller than the Kolmogorov scale, and whose Reynolds numbers remain low. This allows the use of the numerical point-particle formulation, where each particle is tracked as a Lagrangian element and its drag is interpreted as a point force within the carrier phase. This method is successfully used in past studies to probe the effects of a dispersed phase on wall-bounded turbulence.

Pan and Banerjee[16] utilize a numerical method similar to but not considered a point-force method. By accounting for feedback effects through a disturbance velocity (rather than a force), they are able to study the changes in wall-normal settling velocity, particle concentration, and particle size in a turbulent channel flow. They observe both attenuation and enhancement of turbulence with small and large particles, respectively, corresponding to increases and decreases in the frequency of the near-wall ejection-sweep cycle. Li *et al.*[17] examine turbulent channel flow at $Re_\tau = 125$, laden with particles of varying Stokes numbers, mass fractions, and density ratios. For a constant pressure gradient and with a streamwise gravitational force acting on the dispersed phase (i.e., a vertically oriented channel), they find an increase in the bulk flow rate as well as a significant reduction in magnitude of the Reynolds stresses throughout the channel, depending on the particle characteristics. Particle collisions also modify turbulence statistics. Again in a turbulent channel, Mito and Hanratty[18] study entrainment and deposition by injecting and removing particles at the walls (rather than allowing them to elastically collide as is typically done). They observe significant reductions in Reynolds stresses and wall-normal turbulent fluctuations, and interpret the reduction in Reynolds stress as a direct result of the increased feedback force with increasing mass loading. Zhao *et al.*[19] report similar changes to turbulent channel flow, showing an increase in flow rate (at a constant pressure gradient) with a corresponding decrease in Reynolds stress. They show a decrease in the intensity of the turbulent motions, with increased streamwise coherence of near-wall streaks after the addition of a somewhat high loading of solid particles. In a series of studies, Dritselis and Vlachos[20,21] use the point-particle approach with conditional averaging to study how near-wall coherent structures are affected by small particles. They find that by collectively opposing local rotational motion, the elements of the dispersed phase effectively produce a counter-torque within near-wall vortical motions, thereby weakening them and damping wall-normal momentum transport.

As pointed out by Eaton,[22] the point-particle approach is fundamentally limited in that it cannot represent particles interacting with turbulent scales equal to or smaller than their diameter. Present studies are just beginning to fully resolve the flow around individual particles and couple their interaction with the carrier phase. Shao *et al.*[23] recently did this for a turbulent channel flow, and Gao *et al.*[24] and Lucci *et al.*[25] do so for isotropic turbulence. These fully resolved simulations, however, are limited to low density ratios, low Reynolds numbers, and relatively large particles.

The objective of the present study is to determine and explain changes in wall-normal momentum transport with the addition of small spherical particles. This is primarily motivated by the turbulent, spray-laden air/sea interface, where the sensitivity of wall-normal turbulent fluxes to a dispersed phase (i.e., their size, concentration, etc.) needs to be determined in order to predict the surface drag at high winds. Since the density difference between air and water is large, and especially since fully resolving realistic concentrations of spray droplets are prohibitively expensive, the point-particle approximation is used. Turbulent Couette flow, in contrast with the more common pressure-driven channel flow, is employed since the total wall-normal momentum transport is constant with height—a characteristic which is not present in channel flow and allows for unambiguous comparisons between varying dispersed phase conditions. While the present work is motivated by spray suspended above
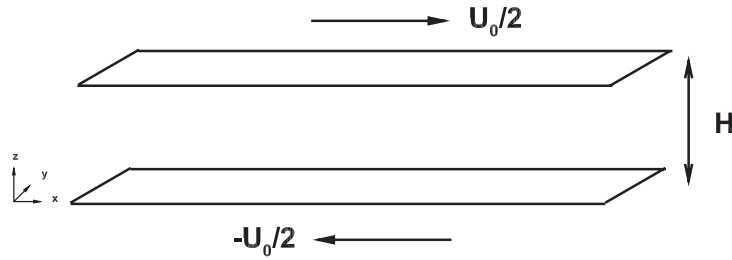
FIG. 1. Schematic of Couette cell geometry. Reference velocity U_0 is the difference in plate velocity and reference length H is the distance between the plates.

the air-sea interface, this article focuses on the fundamental interactions between turbulence and dispersed phases, reserving discussion of the marine boundary layer to other audiences.[26]

II. PROBLEM FORMULATION

A. Carrier phase

The equations governing the carrier phase are the incompressible Navier-Stokes equations, including a particle feedback force in the momentum equations. These include mass conservation,

$$\frac{\partial u_j}{\partial x_j} = 0, \tag{1}$$

and momentum conservation,

$$\frac{\partial u_i}{\partial t} + u_j \frac{\partial u_i}{\partial x_j} = -\frac{1}{\rho_f} \frac{\partial p}{\partial x_i} + \nu_f \frac{\partial u_i}{\partial x_j \partial x_j} + \frac{1}{\rho_f} F_i, \tag{2}$$

where ρ_f is the carrier fluid density, $\nu_f = \mu_f/\rho_f$ is the carrier phase kinematic viscosity, and F_i is a source term representing the modeled transfer of momentum between the carrier and dispersed phases. F_i is computed by summing the collective force felt by particles due to drag within a computational volume; see Sec. II B.

The flow studied is turbulent Couette flow between infinite parallel plates separated by a distance H, represented schematically in Figure 1, where each of the two plates moves at an equal and opposite velocity of $U_0/2$. No-slip boundary conditions are imposed on the carrier phase at the walls, and periodicity is enforced in both the streamwise (x) and spanwise (y) directions. Since the flow is driven by the motion of the plates, no mean pressure gradient exists. The bulk Reynolds number of all simulations is prescribed to be $Re = U_0 H/\nu_f = 8100$.

As noted in the Introduction, the total stress profile in Couette flow is constant with height, even in the presence of a dispersed phase. The total stress, denoted τ throughout, is therefore equal to the wall stress τ_w, and can be used to define the friction velocity $u_\tau = \sqrt{\tau_w/\rho_f}$ and viscous length $\delta_\nu = \nu_f/u_\tau$. This constant stress profile is ideal for monitoring changes to the balance of the momentum flux components across flow regimes with varying types of particles. Note that, as defined above, the bulk Reynolds number does not vary with the addition of a dispersed phase, while the friction Reynolds number ($Re_\tau = u_\tau H/(2\nu_f)$) can change with varying particle effects. The constant-stress profile also mimics the constant-flux layer found in the lower portion of the atmosphere, which is a common assumption when modeling fluxes from the ocean surface in the presence of spray.[4,27]

B. Dispersed phase

Within the carrier phase, the point-particle technique is employed to track and transport the non-interacting elements of the dispersed phase. Each particle is assumed to collide elastically with the domain walls. The point-particle approximation implies that the individual particles are not

explicitly resolved on the mesh, but rather are located at an infinitesimal point and interact with the carrier phase through a point force determined by a drag coefficient and a local slip velocity. This assumption is valid provided several criteria are met: the particle Reynolds number remains $O(1)$ or below; the particle size remains smaller than the smallest scales of the surrounding turbulent flow; and the average distance between particles is large compared to its diameter. The current study, therefore, is valid only for particles which satisfy these conditions. Furthermore, the assumption that the density ratio between the particle and the fluid (ρ_p/ρ_f) is large allows for simplification of the governing dispersed phase equations.[28] Under these assumptions, the equations governing the motion of each particle are

$$\frac{dx_i}{dt} = v_i,\tag{3}$$

$$\frac{dv_i}{dt} = \frac{f_i}{m_p} = \left(1 + 0.15 Re_p^{0.687}\right)\frac{1}{\tau_p}\left(u_{f,i} - v_i\right),\tag{4}$$

where x_i is the location of the point particle; v_i is its velocity; $u_{f,i}$ is the fluid velocity at the particle location; τ_p is the Stokes relaxation time of the particle, defined as $\tau_p = \rho_p d_p^2/18\mu_f$, where ρ_p and d_p are the particle density and diameter, respectively; and Re_p is the particle Reynolds number, defined as $Re_p = |u_{f,i} - v_i|d_p/\nu_f$. The quantity $\left(u_{f,i} - v_i\right)$ is the slip velocity of the particle. The Re_p dependence in Eq. (4) comes from an empirical drag coefficient for a rigid sphere,[29]

$$C_D = \frac{24}{Re_p}\left(1 + 0.15 Re_p^{0.687}\right).\tag{5}$$

This Reynolds number correction to the linear Stokes drag experienced by a solid, spherical particle is valid up to $Re_p \approx 800$.

To dynamically couple the dispersed and carrier phases, the drag force experienced by an individual particle (f_i in Eq. (4)) is related to the momentum source term F_i in Eq. (2). For this study, a projection technique is used (as opposed to the particle-in-cell approach), where the individual force of particle α, $f_{i,\alpha}$, is geometrically projected onto the eight surrounding computational nodes for each particle in the system,

$$F_i^j = -\sum_\alpha \frac{w_\alpha^j}{\Delta V_\alpha} f_{i,\alpha}.\tag{6}$$

In Eq. (6), the summation is over each particle α contained in the total volume created by the union of all eight computational volumes which share node j, and w_α^j is the (dimensionless) linear geometric weight for each particle based on its distance from node j. ΔV_α refers to the volume of the computational cell which the particle lies in. Boivin et al.[30] show that this projection technique, when compared to the particle-in-cell approach, can more fully reconstruct an energy spectrum from the fluid velocities interpolated to the particle location. It is successfully implemented in other complex applications.[2]

By only incorporating a drag force on each particle, other force terms in the equation for motion about a sphere, such as the Basset history force, the Faxen corrections, and the added mass term, are neglected since they remain small compared to drag when the density ratio ρ_p/ρ_f is large. Another simplification is that the particles are assumed not to interact with each other, as the bulk volume fraction remains low (below 10^{-3}) throughout this study. Finally, gravity is also neglected from the equations of particle motion, in order to investigate the interaction between the particles and turbulence absent from the effects of other body forces.

C. Numerical implementation

The structure of Couette flow differs significantly from that of channel flow, primarily due to large rollers spanning roughly 15 channel heights in the streamwise direction which have no direct analogy in boundary layer flow (see, for example, Lee and Kim[31] for a description). The existence of

these structures present numerical difficulties, as illustrated in previous DNS studies by Komminaho et al.[32] and Tsukahara et al.,[33] where domains of large spanwise and streamwise extent (upwards of $[L_x, L_y] = [20H, 8H]$) are required to resolve multiple rollers. In the present case, computational constraints restrict the domain size to be $[L_x, L_y, L_z] = [2\pi H, 2\pi H, H]$. Preliminary tests indicate that particle-laden velocity statistics, particularly the Reynolds stresses, are relatively insensitive to spanwise extent, in agreement with the findings of Tsukahara et al.[33] who show that while two-point correlation statistics are dependent on domain size, turbulent velocity statistics are generally not.

The number of grid points in each direction are $[N_x, N_y, N_z] = [128, 256, 128]$, and these are distributed uniformly in the periodic x and y directions (with $\Delta x = L_x/N_x$ and $\Delta y = L_y/N_y$). The higher resolution in the y (spanwise) direction is required to resolve thin near-wall streaks. In the z direction, algebraic stretching is used to cluster points near the walls, specifying an initial grid spacing of $\Delta z^+_{first} = 1$ (where the superscript $+$ refers to scaling by the viscous length δ_v). In viscous units, $\Delta x^+ = 12.25$, and $\Delta y^+ = 6.125$, while the grid resolution normalized by the Kolmogorov length at the channel centerline is: $[\Delta x/\eta_K, \Delta y/\eta_K, \Delta z/\eta_K] = [4.9, 2.45, 1.5]$. This resolution is adequate for fully resolving the viscous dissipative scales in direct numerical simulation.[34]

The equations governing the carrier fluid phase, Eqs. (1) and (2), are solved numerically using a parallelized large eddy simulation code developed for studying the planetary boundary layer,[35] modified for direct numerical simulation. Spatial discretization is pseudospectral in the x and y directions, and second order finite differences are used for spatial derivatives in the inhomogeneous z direction. Time advancement is accomplished using a low storage, third order Runge-Kutta (RK3) scheme[36] for all terms in the momentum equation where the adaptive time step Δt is determined from a Courant-Friedrichs-Lewy (CFL) number of 0.63. Incompressibility is enforced via a fractional step method, where a pressure Poisson system is solved to guarantee divergence-free velocity fields at each Runge-Kutta stage.

At each time step, in addition to advancing the fluid velocity and pressure, each element of the dispersed phase is integrated according to Eqs. (3) and (4) using the same RK3 time discretization utilized for the carrier phase. Since the particle locations do not coincide with the computational mesh, fifth order Lagrange interpolation is used at each RK3 stage to obtain the fluid velocity at the instantaneous particle location. In the z direction near the walls, this is modified to maintain the highest degree of polynomial while keeping the interpolation stencil symmetric about the particle.

In all simulations, the carrier phase is initialized by the velocity field obtained from a previously simulated unladen case with the particles distributed randomly throughout the domain. The simulations are then run for at least 2.5×10^5 time steps for a total time of at least $tU_0/H \approx 4000$ or $t^+ = tu_\tau/\delta_v \approx 62\,500$.

Finally, validation of the numerical scheme was done in several stages. First, the accuracy of the carrier phase solution was confirmed by comparing to previous simulations of turbulent Couette flow;[33,37,38] particularly, ensuring that mean and fluctuating velocity statistics were faithfully captured. Next, passive particle transport (i.e., one-way coupling) was verified by testing against the benchmark case of Marchioli et al.,[39] and finally, two-way coupling was verified by qualitatively comparing channel flow simulations to existing studies.[17,19,21]

III. PARAMETER CHOICES

Once the non-interacting, point-particle approximation is invoked within the numerical scheme, the system collapses in complexity, and results can only be faithfully compared to physical cases where the necessary conditions of the model are met. For the current case, the primary parameters of interest are the particle Stokes number, defined as the ratio between the particle acceleration time scale and the Kolmogorov time scale at the channel centerline ($St_K = \tau_p/\tau_K$), and the mass loading of particles ϕ_m, defined as the ratio of the particle mass in the system to the carrier phase mass. Individual parameters d_p and ρ_p/ρ_f do not appear independently (except indirectly, as d_p appears in the Reynolds number correction to the drag in Eq. (5)), and are chosen to achieve desired values of St_K and ϕ_m. Attempts to compare the current results to a study such as Tanaka and Eaton,[10] for example, are not possible since they include finite-volume effects of the dispersed phase.
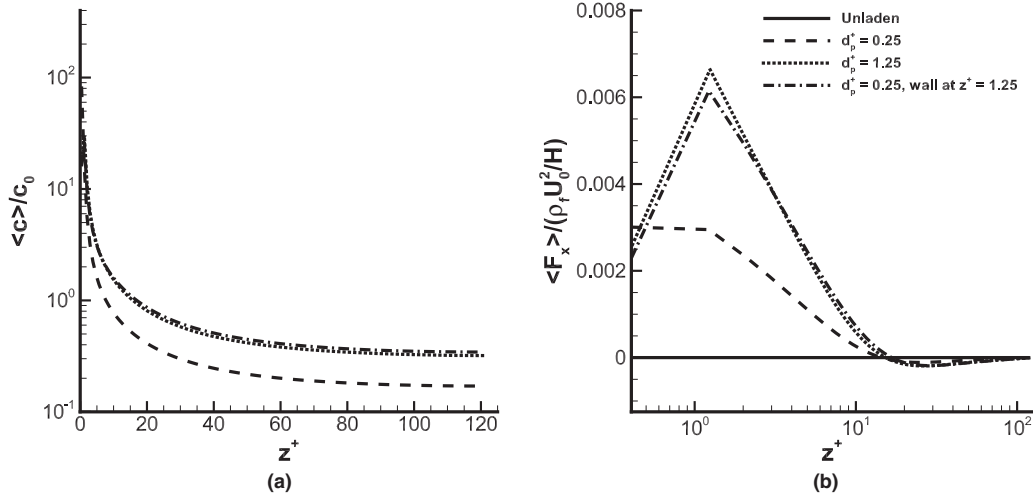
FIG. 2. (a) Normalized mean particle concentration $\langle c \rangle /c_0$ versus z^+, where c_0 is homogeneous bulk particle concentration. (b) Normalized mean particle feedback force, $\langle F_x \rangle /(\rho_f U_0^2/H)$. Curves represent the following: unladen case (solid); small particle, $d_p^+ = 0.25$ (dashed); large particle, $d_p^+ = 1.25$ (dotted); and small particle with the rebound distance specified at $z^+ = 1.25$ (dashed-dotted). All particle-laden runs at $St_K \approx 11$ and $\phi_m = 0.25$.

The particle diameter determines the collision distance from the wall, and this plays an important role in the overall dynamics. Particles with diameters small compared to the viscous length, $d_p^+ \lesssim 1$, tend to "stick" near the walls, with the carrier phase not providing enough wall-normal transport to eject them back into the channel center due to strong viscous effects near the wall. Particles with diameters larger than $d_p^+ \approx 1$, on the other hand, are by definition larger than a viscous wall unit and are therefore more likely to interact with wall-normal turbulent motions. Thus a flow with the same mass fraction and larger d_p^+ will have more particle mass in the bulk of the domain and as a result experience a higher feedback force than those with $d_p^+ < 1$. This is a phenomenon observed experimentally,[40] where wall ejections are not capable of transporting particles from the wall into the flow if d_p^+ is less than roughly 1.3. Since the current simulation model does not contain a lifting force on a particle, the ability of particles to be transported away from the walls is likely reduced.

The particle trapping effect is illustrated in Figure 2, where the normalized particle mass concentration $\langle c \rangle /c_0$ (where c_0 is the bulk homogeneous mass concentration) and normalized carrier feedback force $\langle F_x \rangle /(\rho_f U_0^2/H)$ are shown over the normalized channel half-height for four different simulations. The figure illustrates that for particles with the same St_K and ϕ_m, the rebound distance from the wall can greatly affect the concentration of particles within the channel, and consequently the particle feedback force felt by the carrier phase. The dashed and dashed-dotted curves show the concentration and feedback force for particles with the same specified diameter of $d^+ = 0.25$, except that the dashed-dotted lines correspond to particles which artificially bounce from the walls as though their diameter was $d^+ = 1.25$. The concentration and feedback force are then larger, and nearly exactly equal to a case where the particle diameter is set to be $d^+ = 1.25$ with the same St_K and ϕ_m (dotted lines). In the current simulations, therefore, the particle diameter d^+ is maintained roughly equal to 1.25 in order to eliminate this trapping effect from the different cases.

Table I summarizes the details of our simulations. At a constant value of $St_K \approx 11$, the mass fraction ϕ_m is varied between 0.1, 0.25, and 0.5, and these are designated Runs 1, 2, and 3. At a constant value of $\phi_m = 0.25$, St_K is varied between 1.2, 10.2, and 97.2, and these simulations are designated Runs 4 and 5 (the combination $\phi_m = 0.25$, $St_K = 10.2$ is common between both sets in Run 2). Note that variations in St_K and d_p^+ are due to minor differences in the Kolmogorov time scale τ_K at the channel centerline and the viscous length scale δ_v, respectively. The results shown in Secs. IV and V, therefore, typically include two items: one showing trends with changing St_K while ϕ_m is held constant, and one showing the effects of holding St_K constant and increasing ϕ_m.

TABLE I. Particle-laden simulation parameters. Runs 1–3 maintain relatively constant St_K and vary ϕ_m while Runs 4 and 5 vary St_K at a constant ϕ_m. The particle Stokes number based on wall units, St^+, and the mean particle Reynolds number, $\langle Re_p \rangle$, are included as well for reference. Also indicated are the curve types used for each case in all subsequent plots.

Run	ϕ_m	St_K	ρ_p/ρ_f	d_p^+	St^+	$\langle Re_p \rangle$	Curve
1	0.1	12.6	1000	1.25	89.3	1.7	Dashed
2	0.25	11.7	1000	1.25	88.4	1.5	Dotted
3	0.5	10.2	1000	1.26	89.3	1.3	Dashed–dotted
4	0.25	1.2	100	1.25	8.5	0.5	Long dashed
5	0.25	97.2	8000	1.24	714	3.6	Dashed double-dotted

IV. RESULTS

A. Fluctuating velocities

Figure 3 presents vertical profiles of the root-mean-square (rms) streamwise velocity fluctuations, normalized by U_0. In Figure 3(a), the profiles are shown for increasing values of St_K at $\phi_m = 0.25$. The effect of Stokes number on u'_{rms} is non-monotonic. At the highest St_K the streamwise fluctuations are nearly unaffected across the channel. At the intermediate Stokes number, $St_K = 11.7$, the fluctuations are increased across the entire channel height. The lowest St_K shows a combination of these effects. This behavior is tightly linked to the large Couette rollers as well as the near-wall velocity streaks, and is discussed further in Sec. V. Figure 3(b) presents the same profiles, but for increasing mass loading ϕ_m holding $St_K \approx 11$. Not surprisingly, the increased mass loading enhances the effects over the channel height, and the magnitude of u'_{rms} rises monotonically with ϕ_m. Since particle-particle interactions are ignored, the higher local concentrations act to linearly increase the momentum coupling force. It should be noted that, as Tsukahara *et al.*[33] demonstrate, the large midplane rollers in turbulent Couette flow cause the mid-channel streamwise velocity fluctuations to remain much larger than in turbulent channel flow. Thus it is the behavior of these rollers and how they interact with the particles which dictates the streamwise velocity fluctuations away from the walls.

Figure 4 shows similar profiles for the wall-normal velocity fluctuations, w'_{rms}, where significant reductions are seen in all cases and at all heights. From Figure 4(a), the behavior of w'_{rms} with increasing St_K appears to be non-monotonic as well, assuming that as St_K is lowered below $St_K \approx 1$
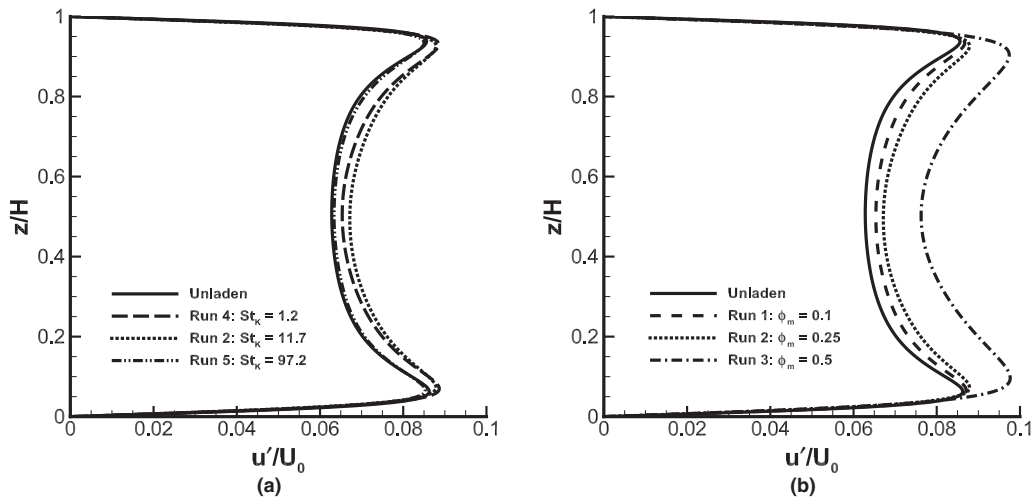

FIG. 3. (a) Fluctuating streamwise velocity profile for varying St_K, holding $\phi_m = 0.25$ constant. (b) Fluctuating streamwise velocity profile for varying ϕ_m, holding $St_K \approx 11$ constant. Fluctuating velocities normalized by plate velocity U_0 and wall-normal position normalized by channel height H.
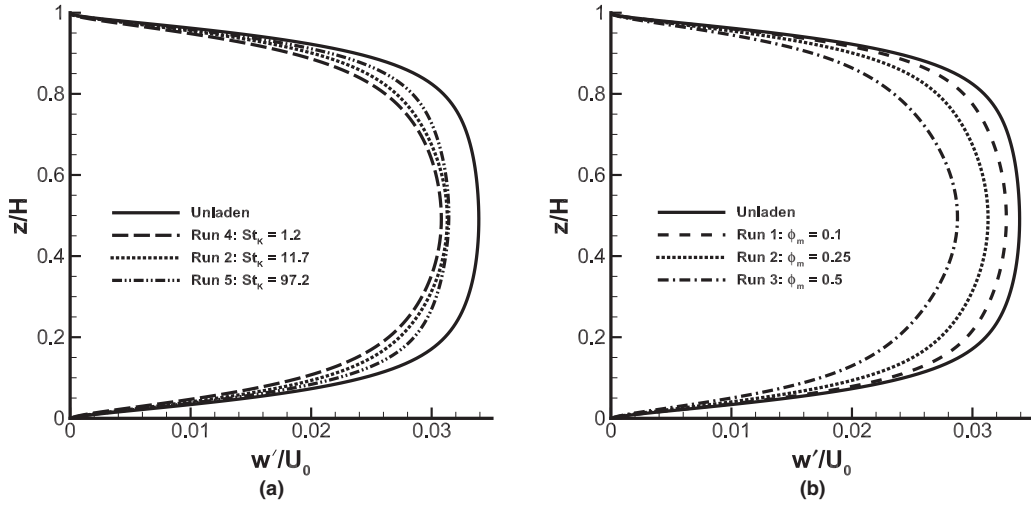
FIG. 4. (a) Fluctuating wall-normal velocity profile for varying St_K, holding $\phi_m = 0.25$ constant. (b) Fluctuating wall-normal velocity profile for varying ϕ_m, holding $St_K \approx 11$ constant. Fluctuating velocities normalized by plate velocity U_0 and wall-normal position normalized by channel height H.

it approaches the unladen profile. Although no additional runs below $St_K = 1.2$ are performed due to computational constraints, it is expected that the maximum effect is centered around $St_K \approx 1$, since previous studies have indicated that particles show maximum preferential concentration in a channel at this Stokes number.[13,41] Other numerical studies have observed similar non-monotonic behavior with changing Stokes number.[17] Figure 4(b) again shows that the decrease of wall-normal velocity fluctuations is enhanced as the mass fraction increases.

This behavior of u'_{rms} and w'_{rms} is in qualitative agreement with previous point-particle simulations in turbulent channel flow. Li et al.,[17] Dritselis and Vlachos,[21] and Zhao et al.[19] all show similar decreases of w'_{rms} and increases of u'_{rms}, despite the differences in flow configuration (channel versus Couette), treatment of gravity, Stokes numbers, mass loadings, and other physical effects (i.e., collisions, etc.). Furthermore, the experiments of Kulick et al.[42] and Righetti and Romano[43] indicate reductions of wall-normal velocity fluctuations, similarly amplified with increasing mass loading. Comparisons of the streamwise velocity fluctuations with the experimental data are not straightforward, however. Kulick et al.[42] show a monotonic decrease in u'_{rms} with mass loading, an effect opposite to the trend in Figure 3(b), but the absence of a streamwise gravitational particle force in the present model can likely explain this discrepancy (the experimental setup of Kulick et al.[42] consisted of a vertically oriented channel), combined with the differences in flow geometry.

B. Turbulent stress

While Figures 3 and 4 give an indication of how the dispersed phase alters the turbulent kinetic energy throughout the Couette geometry, Figure 5 shows profiles of the various components of the total stress. To define each of these components, Reynolds averaging is performed on Eq. (2), where the velocity of each phase is split into mean and fluctuating components ($u_i = \langle U_i \rangle + u'_i$), and spatial averaging is done over the x and y directions (averaging is denoted with $\langle \cdot \rangle$). The averaged streamwise momentum equation for Couette flow with particles is

$$\rho_f \nu_f \frac{\partial^2 \langle U \rangle}{\partial z^2} - \rho_f \frac{\partial}{\partial z} \langle u'w' \rangle + \langle F_x \rangle = 0. \tag{7}$$

One can then define a total stress τ as

$$\tau = \rho_f \langle u'w' \rangle - \rho_f \nu_f \frac{\partial \langle U \rangle}{\partial z} - \int_0^z \langle F_x(z^*) \rangle \, dz^*, \tag{8}$$
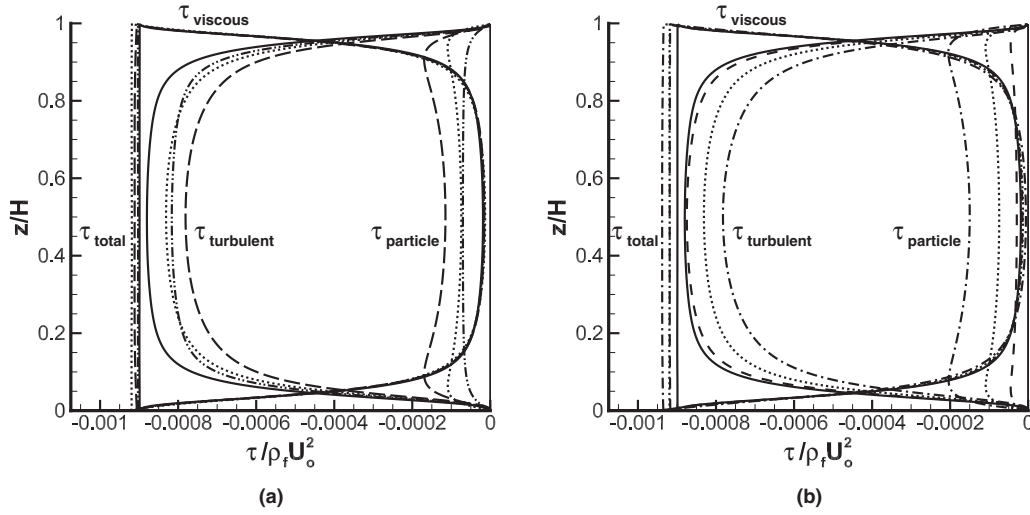
FIG. 5. (a) Profiles of total, viscous, turbulent, and particle stress for varying St_K, holding $\phi_m = 0.25$ constant. (b) Stress profiles for varying ϕ_m, holding $St_K \approx 11$ constant. Stress normalized by $\rho_f U_0^2$ and wall-normal position normalized by channel height H. The curves corresponding to different stress components are indicated on the figures.

which allows Eq. (7) to be written as

$$\frac{\partial \tau}{\partial z} = 0 \Rightarrow \tau(z) = \tau_w, \tag{9}$$

where τ_w is the value of the total stress at the wall, and thus the total stress is constant with height.

Equation (8) shows that the total stress is the sum of the usual components and a new stress due to the coupling between the carrier and dispersed phases. This stress component is a vertical integral of the mean streamwise particle force $\langle F_x \rangle$.

Inspecting Figure 5, it is clear that the total stress does in fact remain constant over the channel height for all simulations. For the unladen case, as is typical for wall-bounded flows, the stress balance shows viscous stress dominating near the walls, while turbulent stress dominates above $z^+ \approx 15$. When introducing a dispersed phase, however, this balance is modified by the additional particle stress.

Figure 5(a) displays the stress profiles, normalized by $\rho_f U_0^2$, for varying St_K at a constant $\phi_m = 0.25$. First, the viscous stress remains nearly unchanged, regardless of the particle Stokes number, implying that the mean velocity profile is nearly unchanged as well. Second, the turbulent stress contribution can be significantly reduced in magnitude, with a maximum reduction of about 12% at the lowest St_K considered. As with the behavior of u'_{rms}, the reduction of $\langle u'w' \rangle$ magnitude appears to be non-monotonic, with a maximum around $St_K \approx 1$. This reduction of the turbulent stress is nearly offset by a rise in the particle stress, resulting in a total stress which varies only slightly with St_K. Since both the turbulent and particle stresses decay to zero at the wall, the small change in total stress is indicative of the minor changes in the mean velocity profile at the wall. Note that there is no theoretical constraint guaranteeing this near-constancy of the total stress, since changes to the mean velocity profile may be brought about by particle interactions.

Figure 5(b) shows the behavior of the stress components with varying mass fraction, holding $St_K \approx 11$. As with u'_{rms} and w'_{rms}, the reduction in the magnitude of $\langle u'w' \rangle$ and subsequent rise of particle stress is amplified nearly linearly with increases in particle concentration. In this case, as the mass fraction of the dispersed phase is increased, the total stress increases by roughly 4%. As in the case of the fluctuating velocities, the reduction of $\langle u'w' \rangle$ magnitude over the channel height with the addition of a dispersed phase has been observed both experimentally and numerically for turbulent wall-bounded flows.[17–19,43]

Physically, this behavior indicates that while the total momentum transfer from the bottom plate to the top plate remains constant within 4%, the transfer by the turbulent carrier phase motion is

significantly reduced by the presence of a dispersed phase, implying a change in the structural nature of the near-wall turbulence. This reduction is offset by the dispersed phase contributing up to 15% of the total momentum transfer, an effect which increases monotonically with dispersed phase mass fraction ϕ_m and non-monotonically with St_K.

At this point, it is instructive to further explore the particle stress, following a procedure outlined nicely by Mito and Hanratty,[18] where the momentum balance of the dispersed phase is analyzed. When describing a dispersed phase as a continuous field, a momentum balance yields

$$\frac{\partial}{\partial t}\left(cv_i\right) + \frac{\partial}{\partial x_j}\left(cv_i v_j\right) = -F_i. \tag{10}$$

Here, c refers to the local, instantaneous particle mass concentration, v_i refers to the dispersed phase velocity, and F_i is the local force per unit volume found in Eq. (2) coupling the two phases. In this formulation, the instantaneous local concentration c is binary (equal to 0 inside the carrier phase or ρ_p inside the dispersed phase) since the carrier and dispersed phases do not mix. Note the momentum source for the dispersed phase is merely the negative momentum source for the carrier phase.

Performing the Reynolds averaging procedure on Eq. (10) and writing only the expression for the streamwise component leads to

$$\frac{\partial}{\partial z}\left[\langle u_p\rangle\langle cw'_p\rangle + \langle cu'_p w'_p\rangle\right] = -\langle F_x\rangle. \tag{11}$$

Now, if the left hand side is instead written with averages taken only over the dispersed phase (or, equivalently, writing in terms of concentration-weighted averages), Eq. (11) becomes

$$\frac{\partial}{\partial z}\langle c\rangle\langle u'_p w'_p\rangle_c = -\langle F_x\rangle, \tag{12}$$

where $\langle\cdot\rangle_c$ denotes a concentration-weighted average. It should be pointed out that since F_i, the force per unit volume which appears in the momentum equations, has been computed via Eq. (6) as a projection of the individual values of f_i for each particle, the concentration dependence of this term has already been implicitly accounted for (hence why the right hand side of Eq. (12) does not contain the dispersed phase concentration).

Integrating over the wall-normal direction then leads to the expression

$$\langle c\rangle\langle u'_p w'_p\rangle_c = \int_0^z -\langle F_x(z^*)\rangle dz^* \equiv \tau_{particle}. \tag{13}$$

Thus the particle stress of Eq. (8) can be written in terms of the fluctuating particle velocities. Recalling from Figure 5 that losses in turbulent transport via the carrier phase Reynolds stress $\langle u'w'\rangle$ are almost fully compensated by increases in the particle stress, Eq. (13) physically states that this new particle stress is in essence the Reynolds stress of the dispersed phase. Furthermore, Eq. (13) indicates that it is possible to experimentally measure $\tau_{particle}$ by computing particle statistics via methods such as phase-Doppler anemometry.

The picture that develops is one where the presence of inertial particles (greater than or equal to a Stokes number of about 1) at moderate mass loadings can significantly change the nature of the carrier phase flow. While the total stress remains constant within 4% over the simulations performed, the partitioning of this transfer between the carrier and dispersed phase is highly sensitive to both the particle Stokes number and the mass loading. Since the carrier phase Reynolds stress is reduced, this implies significant changes to the flow turbulence, as indicated by the profiles of u'_{rms} and w'_{rms} in Figures 3 and 4. These changes and their dependence on St_K and ϕ_m are discussed in Sec. V.

V. DISCUSSION

A. Fluctuating velocities

Figure 3 shows that in general, particularly for the case with high mass loading, u'_{rms} is increased across much of the Couette cell height. This increase in the streamwise variance is in sharp contrast to the decreases in magnitudes of v'_{rms} (not shown), w'_{rms} (Figure 4), and $\langle u'w'\rangle$ (Figure 5). By viewing a
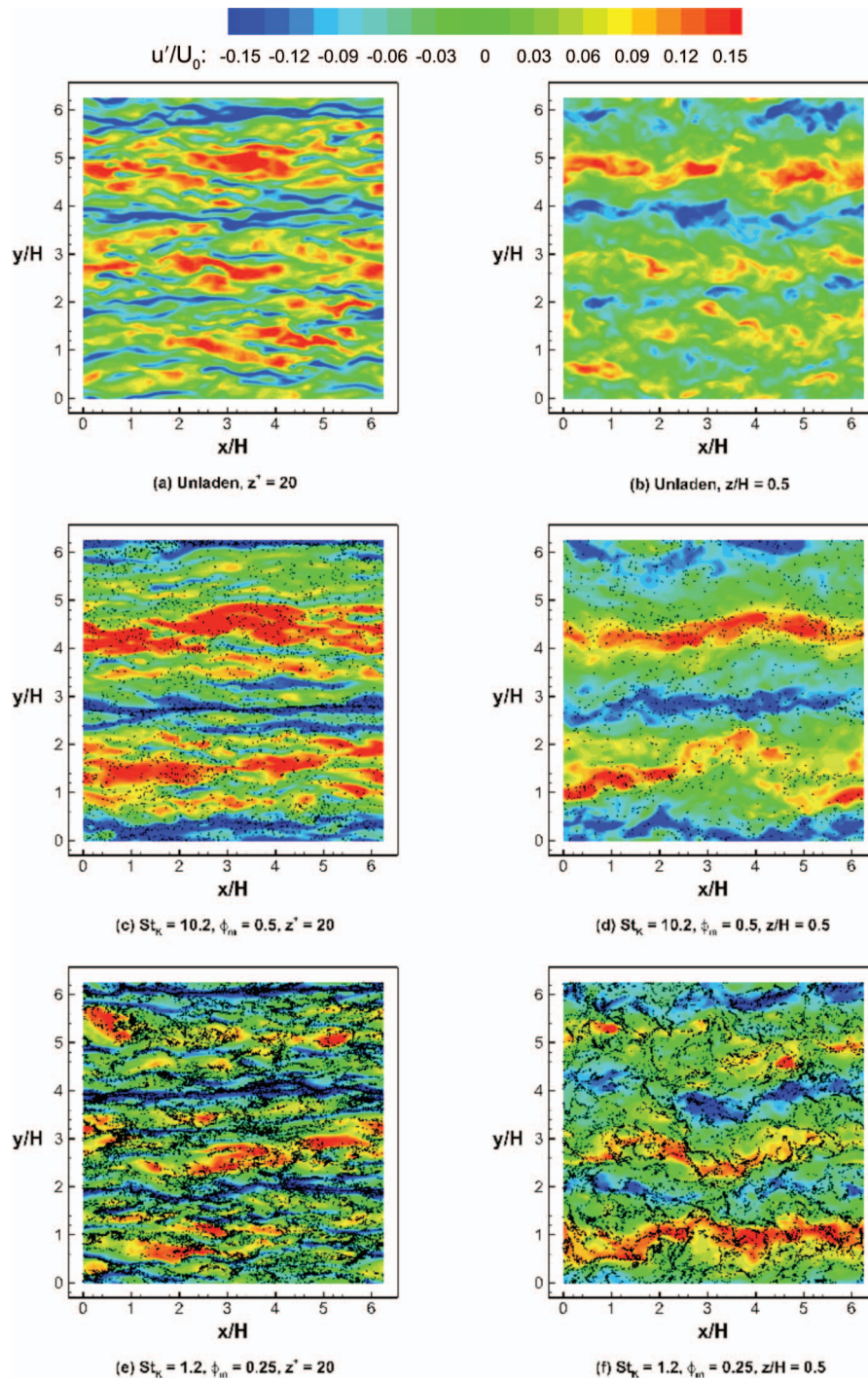
FIG. 6. Instantaneous snapshots of normalized fluctuating streamwise velocity u'/U_0 with particle locations (black dots) for the following cases: unladen (top row); Run 3: $St_K = 10.2$, $\phi_m = 0.5$ (middle row); and Run 4: $St_K = 1.2$, $\phi_m = 0.25$ (bottom row). Left column is at a location of $z^+ = 20$ and right column is at the channel midplane: $z/H = 0.5$. Note that particle sizes have been magnified and thus are not to scale.

snapshot of an instantaneous field of the fluctuating velocity u', the reason for this increase becomes clear. Figure 6 shows contours of u'/U_0 in an x-y plane, along with dots representing instantaneous particle locations, at two different heights: $z^+ = 20$ (near the peak location of u'_{rms}) and $z/H = 0.5$ (the centerline). The unladen case is compared to the two cases with the highest degree of turbulence

modification: the high mass loading case (Run 3: $St_K = 10.2$, $\phi_m = 0.5$) and the low St_K case (Run 4: $St_K = 1.2$, $\phi_m = 0.25$).

The velocity contours in this figure show that the flow is significantly altered by the presence of the dispersed phase. Near the wall (left column), the high- and low-speed streaks appear both longer and stronger in the streamwise direction for the laden cases, particularly for high mass loading. These strengthened streaks correlate more coherently with the large mid-plane rollers located directly above (seen on the right column). At the channel midplane, these rollers become noticeably stronger and coherent as well, with a general decrease in small-scale turbulence. This visual evidence is stronger for the $\phi_m = 0.5$, $St_K = 10.2$ case (Figures 6(c) and 6(d)) than for the lower St_K case at $\phi_m = 0.25$ (Figures 6(e) and 6(f)). The increase of streamwise velocity fluctuations seen in Figure 3 results from the strengthening of the midplane rollers and near-wall streaks, despite the visual reduction of small-scale turbulence and the decrease of v'_{rms} and w'_{rms}.

This increased near-wall streak coherency and subsequent rise in u'_{rms} has been previously observed for particle-laden flows. Zhao et al.[19] numerically studied a turbulent channel flow with a large mass loading ($\phi_m = 1.0$) and moderate Stokes number ($St^+ = 30$), and found not only a similar increase of the u'_{rms} profile and decrease of the v'_{rms} and w'_{rms} profiles, but a similar qualitative change to the near-wall streaks as well (without the effects of the midplane rollers). These streaks become longer in streamwise extent, more intense, and wider in spanwise wavelength. As the authors point out,[19] this change to the near-wall turbulence shares the same qualitative behavior as turbulent channel flow in the presence of drag-reducing polymer additives.[44]

To examine this behavior more quantitatively, normalized energy spectra $E_{11}(k_y)$ as a function of the spanwise wavenumber k_y are shown in Figure 7 for all cases at the same heights shown in Figure 6. Among these spectra, two distinguishing features stand out. First, energy contained near the dissipative scales is generally diminished for all cases at both heights—an effect qualitatively observed in Figure 6. This behavior is monotonic with increasing ϕ_m and maximized at $St_K = 1.2$. Second, energy at the low wavenumber end of the spectrum generally increases with the addition of particles. With increasing mass fraction, the peak in the spectrum shifts to lower wavenumbers, and becomes more energetic at both heights. As a function of St_K, the energy at low wavenumbers is increased as well, with a maximum at $St_K = 1.2$. In the limit of high Stokes number, the energy spectra at low wavenumbers remain nearly unchanged. This pattern of more energetic, lower wavenumber structures of u' in the spanwise direction is indicative of the strengthening and widening of both the midplane rollers and near-wall streaks as seen in Figure 6. Since the near-wall streaks are heavily influenced by the presence of the midplane rollers, the wavenumber associated with the roller spacing is manifested as a peak in the energy spectrum throughout the entire channel height.

In their experimental study, Kulick et al.[42] showed that with the addition of copper particles, changes to the streamwise energy spectra $E_{11}(k_x)$ were in qualitative contrast with the present results (note that spectra in Figure 7 are in the spanwise direction; streamwise spectra $E_{11}(k_x)$ exhibited similar high-wavenumber behavior with particle effects and are not shown here). Depending on the mass loading, energy attenuation was found to be particularly pronounced in distinct frequency bands—a phenomena also in contrast to previous wall-bound experimental results.[45,46] The disparity in Reynolds number (and therefore the ratio of the largest to smallest length scales) between feasible simulations and typical experimental setups prevents a further examination of this effect, and therefore the question of how particles under the point-particle approximation manifest their presence in energy spectra of high-Reynolds number, wall-bounded flows remains open until additional simulations are performed. It is worthwhile to note that the spectra shown in Figure 7 are in qualitative disagreement with energy spectra taken from several numerical studies of isotropic, particle-laden turbulence. In many of the spectra reviewed by Poelma and Ooms,[47] a "crossover wavenumber" was observed, beyond which the dispersed phase (of Stokes number $O(1)$) enhances energy content. Only at sufficiently high St_K do these studies begin to see energy suppression at high wavenumbers. In the current simulations, we do not observe any degree of turbulence augmentation at high wavenumbers, even at the lowest probed Stokes number, highlighting the fundamental differences between wall-bounded and homogeneous turbulence and its response to inertial particles. The order-of-magnitude differences between St_K and St^+ illustrate this fact (see Table I), and the physical mechanisms described in the various studies reviewed by Poelma and Ooms[47] explaining
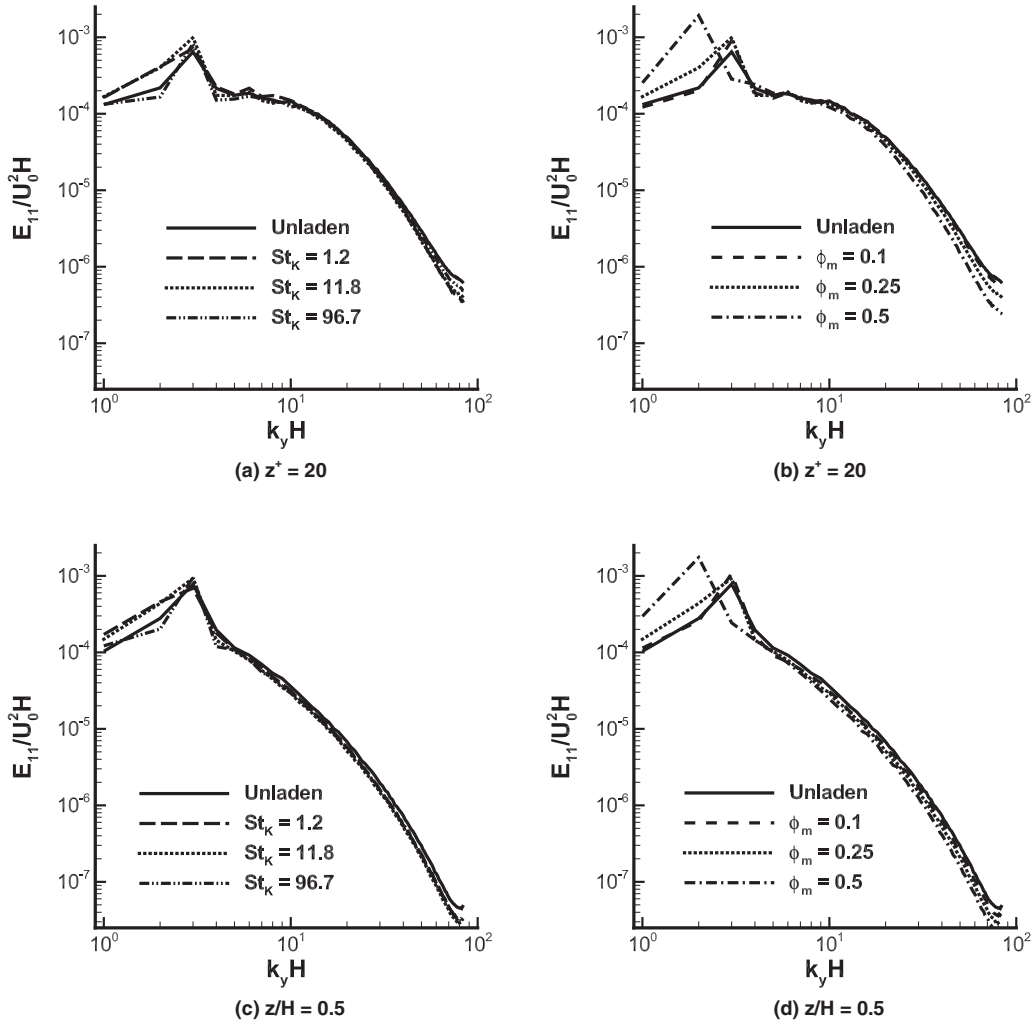
FIG. 7. Energy spectra E_{11} taken in the spanwise direction (k_y) for all cases. Top row is spectra at a height of $z^+ = 20$ and bottom row is spectra at the channel midplane: $z/H = 0.5$. (a) and (c) Comparison of cases holding ϕ_m constant at 0.25. (b) and (d) Comparison of cases holding $St_K \approx 11$ and varying ϕ_m

the enhanced small-scale energy do not necessarily apply in wall-bounded turbulence with mean gradients.

Focusing now on the distribution of particles, Figure 6 qualitatively demonstrates that particles with $St_K = 1.2$ have a greater tendency to collect in regions loosely corresponding to smaller scale turbulent structures (e.g., the near-wall, low-speed streaks), while particles with $St_K = 10.2$ tend to accumulate in regions associated with the large midplane rollers. The probability density function of the streamwise velocity fluctuation seen by the particle (u'_f, the carrier phase velocity fluctuation at the particle location) for all particles within the range $10 \leq z^+ \leq 20$ is shown in Figure 8. The probability density function for the $St_K = 10.2$ case exhibits two peaks: one broad peak centered slightly on the negative side of the $u'_f/U_0 = 0$ axis, and one sharper peak near $u'_f/U_0 \approx -0.2$. The sharp peak at $u'_f/U_0 \approx -0.2$ corresponds to a large number of particles residing in the large, low-speed regions associated with the midplane rollers. For the $St_K = 1.2$ case, however, Figure 8 shows that these particles, on average, experience a broader range of negative streamwise velocity fluctuation, exhibiting only one broad peak centered around $u'_f/U_0 \approx -0.07$. The lack of a sharp peak associated with the midplane rollers indicates that while they still tend to accumulate in low-speed regions near the wall (the mean value of u'_f/U_0 is negative), their distribution is more
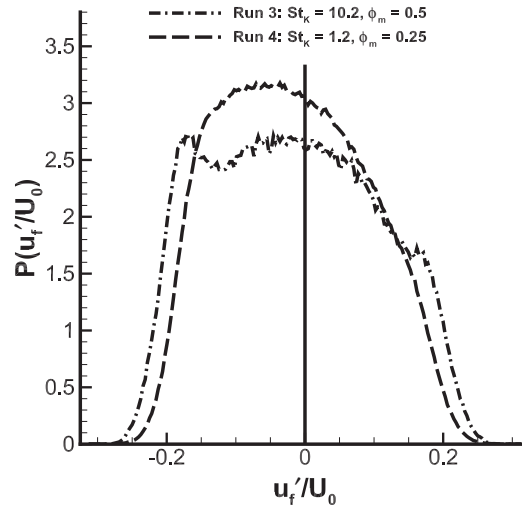
FIG. 8. Probability density function of the fluctuating streamwise velocity, computed at the particle location, for all particles within range $10 \leq z^+ \leq 20$. Two curves are shown: Run 3 ($St_K = 10.2$, $\phi_m = 0.5$) and Run 4 ($St_K = 1.2$, $\phi_m = 0.25$)

widespread since they preferentially concentrate on smaller scales than the $St_K = 10.2$ particles, and not necessarily in streaks corresponding to the midplane rollers.

This difference in the spatial scale of particle clustering at different St_K is entirely due to the acceleration time scale of the particle, and the preferential concentration observed in the system can be predicted by estimating relevant local time scales. As will be shown later, the streamwise vortices associated with near-wall velocity streaks have a characteristic nondimensional vorticity on the order of $\omega_{nw} H / U_0 \approx 1.25$, leading to a characteristic time scale of $\tau_{nw} U_0 / H \approx 0.8$. This is approximately equal to the nondimensional particle time scale for the $St_K = 1.2$ case, leading to a local Stokes number (based on the characteristic vorticity of the near-wall structures) of approximately 1. Previous studies show[13] that particles with a Stokes number of 1 approach a maximum in preferential concentration. Therefore, the $St_K = 1.2$ particles accumulate in the low-vorticity, high-strain-rate regions associated with the spatial scales of the near-wall vortices. Larger particles, however ($St_K = 10.2$), do not display this small-scale segregation, but rather collect in near-wall regions associated with the convergence zones of the large-scale midplane rollers. By estimating the vorticity of these rollers from the maximum value of the wall-normal velocity and the channel height, it is found that the nondimensional time scale for the midplane rollers is roughly $\tau_{mpr} H / U_0 \approx 2$. The time scale for the $St_K = 10.2$ particles is roughly the same (≈ 2), thus these larger particles preferentially concentrate in response to motion of the midplane rollers, not the near-wall streaks. At still higher Stokes numbers, the concentration of particles merely appears homogeneous (not shown).

Physically, therefore, it appears that as the particle time scale is increased, the spatial scale on which they preferentially concentrate increases as well, from the near-wall vortical structures to the large midplane rollers. This adjustment of the particle clustering length scale with changing Stokes number is discussed from a theoretical basis in other studies.[48,49] The smaller particles therefore "operate" on scales associated with the near-wall streaks while the larger particles do so on the larger structures. While the higher St_K particles collect in the large-scale regions associated with midplane rollers, their trajectory is more or less unaffected by smaller scale motions, which as a result dampens small-scale turbulent fluctuations. What appears to occur, therefore, is the same process on two different spatial scales: just as the $St_K = 1.2$ particles cause the near-wall streaks to become more coherent and damp wall-normal fluctuations, the $St_K = 10.2$ particles do the same to the midplane rollers, strengthening their streamwise coherence while at the same time damping all fluctuating motions occurring at smaller time scales.
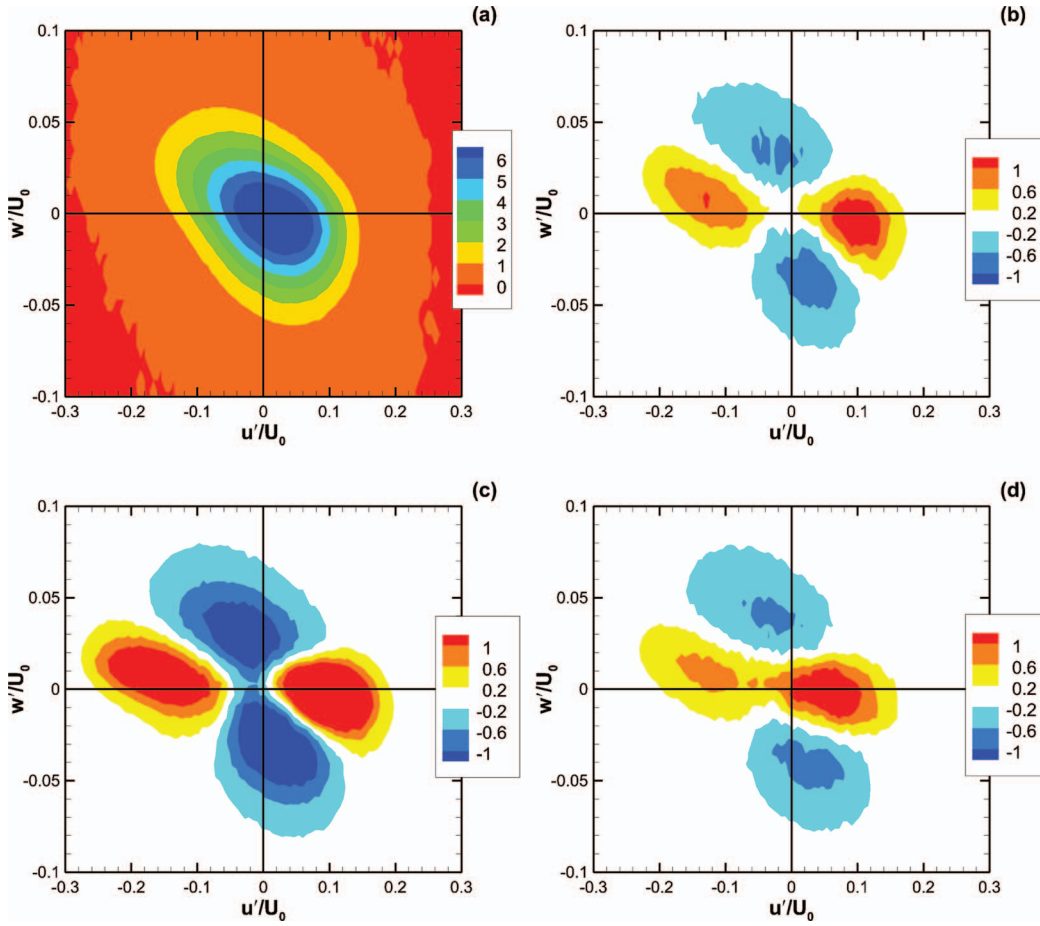
FIG. 9. (a) Joint probably distribution function of streamwise (u') and wall-normal (w') velocity fluctuations at a height of $z^+ = 40$. Panels (b)–(d) show difference between laden and unladen cases: $P_{diff}(u', w') = P_{laden}(u', w') - P_{unladen}(u', w')$. (b) $St_K = 11.7$, $\phi_m = 0.25$ (Run 2); (c) $St_K = 10.2$, $\phi_m = 0.5$ (Run 3); and (d) $St_K = 1.2$, $\phi_m = 0.25$ (Run 4). Note that the u' and w' axes use different scales.

B. Near-wall turbulent transport

This naturally leads to a discussion of the stress profiles presented in Figure 5, where momentum transport due to turbulent carrier phase motions is significantly reduced while compensated almost completely by a rise in the magnitude of the particle stress $\tau_{particle}$. It has been argued[50] that the majority of the Reynolds stress $\langle u'w' \rangle$ near the wall is due to "bursting" and "sweeping" events, as evidenced by joint probably density functions of u' and w' dominated by the anticorrelated 2nd and 4th quadrants (where their product is negative). The hairpin model of near-wall structures is consistent with this statistical description, where streamwise vortices join to form a head, then lift from the wall.[51] In the present context, how does the dispersed phase alter these near-wall vortical structures which are primarily responsible for turbulent transport? In answering this, the behavior observed in Figure 5 can be properly explained.

Figure 9 shows joint probability distribution functions of u' and w' at $z^+ = 40$ for the unladen case, along with the differences between three laden cases and the unladen case: Two mass fractions at roughly the same St_K (Run 2: $St_K = 11.7$, $\phi_m = 0.25$; Run 3: $St_K = 10.2$, $\phi_m = 0.5$) and the low St_K case (Run 4: $St_K = 1.2$, $\phi_m = 0.25$). Clearly, for the uncoupled case (Figure 9(a)), the probability distribution is skewed in a way that emphasizes events in the 2nd and 4th quadrants, in agreement with the above description of sweeps and bursts. With the addition of particles of Stokes number roughly equal to 10, the probability of events lying in these quadrants decreases with increasing mass fraction, seen in Figures 9(b) and 9(c). This is fully consistent with the monotonic decrease
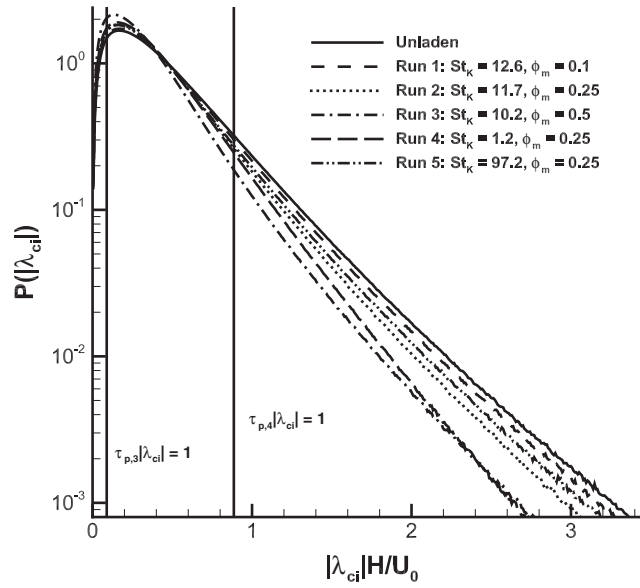
FIG. 10. Probability density function of the nondimensionalized swirling strength, $|\lambda_{ci}|H/U_0$. All laden cases are included as well as the unladen case. Vertical lines represent the point where the time scale of the swirling motion (inverse of $|\lambda_{ci}|$) is equal to the acceleration time scale of particles from Run 3 ($\tau_{p,3}$) and Run 4 ($\tau_{p,4}$).

of the turbulent Reynolds stress magnitude found in Figure 5(a) with increasing mass fraction. The increases along the $w' = 0$ axis are indicative of the increase in strength of the near-wall streaks, seen in Figure 3. Similarly, the decreases along the $u' = 0$ axis illustrate the decrease in levels of wall-normal velocity fluctuations seen in Figure 4. It should be emphasized that not only are the levels of u' and w' changed (Figures 3 and 4), but the correlations between these fluctuating events are changed with particle mass fraction as well. The change in correlation is confirmed by observing that the correlation coefficient $\langle u'w' \rangle / \left(\langle u'^2 \rangle^{1/2} \langle w'^2 \rangle^{1/2} \right)$ decreases in the same way as the Reynolds stress $\langle u'w' \rangle$ in Figure 5 (not shown).

For the low St_K particle case, some explanation is required. Qualitatively, the change in the joint probability distribution function (Figure 9(d)) looks much like that for the $St_K = 11.7$ case at the same ϕ_m. This is despite the fact that, as shown in Figure 5(b), the reduction in turbulent momentum transport is noticeably larger for the $St_K = 1.2$ case compared to the $St_K = 11.7$ case. It would therefore appear that even with relatively little change to the joint probability function of u' and w', particles with $St_K \approx 1$ can, at the same mass fraction, reduce turbulent transport more effectively. This would indicate that any changes in turbulent structure would be in events of u' or w' that do not contribute strongly to the joint probability distribution.

To examine the events responsible for sweep and ejection processes, the local "swirling strength" $|\lambda_{ci}|$, is used, which is mathematically defined as the magnitude of the imaginary part of the complex eigenvalue of the local velocity gradient tensor. This quantity is proposed by Zhou *et al.*[52] for visualizing hairpin structures in a turbulent channel flow. Figure 10 shows probability distribution functions of $|\lambda_{ci}|H/U_0$ over the entire domain. Not surprisingly, the figure shows that increasing the mass fraction at $St_K \approx 11$ results in a monotonic reduction of $|\lambda_{ci}|$ events, above $|\lambda_{ci}|H/U_0$ equal to about 0.5.

For the low Stokes number case, however, a transition can be seen in Figure 10. Below $|\lambda_{ci}|H/U_0 \approx 1.5$, the number of swirling events is similar to the $St_K = 11.7$ case at the same ϕ_m. Above this value, however, the distribution function falls off more steeply with increasing $|\lambda_{ci}|H/U_0$, eventually joining that for the high ϕ_m case around $|\lambda_{ci}|H/U_0 \approx 2.25$. This indicates that the low Stokes number particles are reducing the number of high-$|\lambda_{ci}|$ events more effectively than lower $|\lambda_{ci}|$ events. The fact that low Stokes number particles are transported by weaker swirling motions but resist stronger swirling motions explains this behavior. In Figure 10, two vertical lines are included: one illustrating

where the time scale of the vortical motions (given by the inverse of $|\lambda_{ci}|$) equals the particle acceleration time scale for the $St_K = 11.7$ case (Run 3, $\tau_{p,3}$), and the same for the $St_K = 1.2$ case (Run 4, $\tau_{p,4}$). For $St_K > 10$, all vortical motions identified by $|\lambda_{ci}|$ occur on faster time scales, and thus must work to accelerate any nearby particles. As a result, the number of events at all swirling strengths is reduced uniformly across the entire range of applicable $|\lambda_{ci}|$ (to the right of the leftmost vertical line). For the $St_K = 1.2$ case, however, only beyond the rightmost vertical line, where the vortical motions occur on faster time scales than the particle acceleration time scale, do the number of swirling events decay as much as those for the high ϕ_m case. This dampening of near-wall structures is corroborated by the experiments of Rashidi *et al.*,[53] who, by studying a turbulent particle-laden boundary layer, conclude that while bursting events from the wall were no stronger or weaker in the presence of small particles, they were less frequent, and this resulted in a net reduction of turbulent transport to/from the wall. Furthermore, Righetti and Romano[43] observe that in a turbulent open channel, the intensity (time-weighted contribution from a particular quadrant) of quadrants 2 and 4, particularly for quadrant 2, is diminished in the presence of particles above $z^+ \approx 20$. This is in qualitative agreement with the present results.

A mechanistic explanation provides the reasoning behind how particles can reduce the number of high-strength swirling events. Dritselis and Vlachos[20,21] studied particle-laden channel flows and used conditional averaging to investigate how particles interact with near-wall vortices. They found that particles residing in vortical regions provide a torque opposite to the carrier phase motion since each particle must be accelerated by the surrounding fluid. This opposing torque weakens the conditionally averaged near-wall, quasistreamwise vortex, and increases its diameter in the process. If the particle Stokes number is too low, it will merely travel with the vortical motion and the torque exerted on the carrier phase will weaken. Furthermore, the analytic study by Druzhinin[54] showed similar results: particles centrifuged out of an idealized vortical flow weaken the vortex through drag while retreating to regions of high strain.

Ultimately, the physical picture is proposed as follows. In general, a single inertial (large St_K) particle, when confronted with a carrier phase velocity fluctuation of a time scale shorter than the particle's acceleration time scale (either as part of a coherent motion or not), will tend to remain on a straight trajectory, damping the strength of the fluctuation through the particle's drag. Assuming for the moment a homogeneous concentration of particles, an increase in their number will lead to increased feedback forces everywhere, reflected by the addition of the substantial particle stress across the geometry height. This was clearly seen in Figure 5(b) for increases in ϕ_m at a nearly constant $St_K \approx 11$. For this St_K and higher, the particles are in fact nearly homogeneous in *x-y* planes, with the exception that $St_K \approx 11$ particles still preferentially concentrate in the regions associated with convergence regions of the midplane rollers. As far as the near-wall streaks are concerned, however, these heavy particles are nearly uniformly distributed.

For lower St_K particles, the picture becomes more interesting. Figures 6(e) and 6(f) show that these smaller particles preferentially concentrate on the scales associated with the near-wall, low-speed streaks. So despite the lower bulk concentration, and despite only being able to resist motions of time scales 10 times smaller than the $St_K = 11.7$ case, this local enhancement results in high-strength vortical structures being damped in nearly the same way as a higher bulk mass loading (Run 3). In this way, particle modification of near-wall turbulent motions is optimized when particles preferentially concentrate on length scales equal to those responsible for wall-normal momentum transfer. With too little preferential concentration (high St_K), the particles remain homogeneously distributed and are, on average, not efficiently located in regions where they can impact wall-normal momentum transport. This is illustrated by Run 5, where $St_K = 97.2$. With very low St_K, however, the particles travel with the flow and thus produce zero feedback effect.

Finally, this says nothing of the consequences of adding other physical processes not included in the numerical model, such as particle collisions, gravity, or finite-diameter effects. These have been investigated in other studies,[21,23] and modify this simple physical picture. For example, the high degree of preferential concentration in the $St_K = 1.2$ case leads to maximum volume concentrations which in some cases can approach $O(1)$ locally within the domain. In these highly localized regions, the non-interacting assumption of these point-particles is violated, and the effect of particle collisions needs to be considered. Previous studies, such as that by Dritselis and Vlachos[21] indicate that

particle collisions enhance the turbulence modification seen with the addition of the dispersed phase. Generally speaking, however, we anticipate that the present description of turbulence-attenuating particles can provide a foundation toward building further understanding.

VI. CONCLUSIONS

Simulations of particle-laden turbulent Couette flow are performed to investigate and explain the feedback effects of a dispersed phase on a turbulent carrier phase. The wall-normal transfer of momentum is of primary interest. By limiting our study to particles which meet the requirements for the point-particle approximation (i.e., low volume fraction, no particle-particle interactions, small particle size compared to the smallest turbulent scales), we are able to probe the space of particle Stokes number and mass fraction, as these are the primary parameters of interest under these restrictions.

Turbulence modification is qualitatively similar to previous experimental and numerical studies of wall-bounded turbulent flows. A strengthening of the near-wall streaks leads to an increase in the streamwise fluctuating velocity (u'_{rms}), while spanwise and wall-normal velocity fluctuations are damped. Furthermore, the magnitude of the turbulent Reynolds stress decreases significantly for certain cases, and is counterbalanced by a stress carried by the dispersed phase. The end result is a total momentum transfer which remains nearly the same for all particle parameters studied, but where the contribution from turbulent motions can significantly diminish. This reduction of turbulent transport is found to arise from a weakening and damping of near-wall turbulent structures, and the effectiveness of the particles to achieve this rely heavily on the ability of the particles to concentrate locally.

Since particle-particle interactions are neglected, the increase of the bulk mass fraction ϕ_m typically enhances each observed effect. The behavior as a function of Stokes number, however, does not display this monotonic relationship, since preferential concentration plays a critical role. Because the time scale of the $St_K = 1.2$ particles is of the same order as the time scales of the near-wall vortices, they efficiently weaken these motions compared to particles with longer time scales because they cluster on these scales, leading to high local concentrations and therefore high local feedback forces. Particles with increasing Stokes numbers cannot preferentially concentrate at these length and time scales (they cluster at larger length scales, as seen by the $St_K \approx 11$ particles), which does not lead to the same decrease in the near-wall structures responsible for turbulent transport. Particles with lower Stokes numbers, on the other hand, merely travel with the near-wall motions, resulting in decreasing feedback forces as the Stokes number approaches zero.

ACKNOWLEDGMENTS

[1] M. Cantero, M. Shringarpure, and S. Balachandar, "Towards a universal criteria for turbulence suppression in dilute turbidity currents with non-cohesive sediments," Geophys. Res. Lett. **39**, L14603, doi:10.1029/2012GL052514 (2012).

[2] R. Miller and J. Bellan, "Direct numerical simulation of a confined three-dimensional gas mixing layer with one evaporating hydrocarbon-droplet-laden stream," J. Fluid Mech. **384**, 293–338 (1999).

[3] W. Grabowski and L.-P. Wang, "Growth of cloud droplets in a turbulent environment," Ann. Rev. Fluid Mech. **45**, 293–324 (2013).

[4] E. Andreas, "Spray stress revisited," J. Phys. Oceanogr. **34**(6), 1429–1440 (2004).

[5] E. Andreas and K. Emanuel, "Effects of sea spray on tropical cyclone intensity," J. Atmos. Sci. **58**, 3741–3751 (2001).

[6] L. Bianco, J.-W. Bao, C. W. Fairall, and S. A. Michelson, "Impact of sea-spray on the atmospheric surface layer," Boundary-Layer Meteorol. **140**, 361–381 (2011).

[7] M. Bell, M. Montgomery, and K. Emanuel, "Air-sea enthalpy and momentum exchange at major hurricane wind speeds observed during CBLAST," J. Atmos. Sci. **69**, 3197–3222 (2012).

[8] R. A. Gore and C. T. Crowe, "Effect of particle size on modulating turbulence intensity," Int. J. Multiphase Flow **15**, 279–285 (1989).

[9] G. Hetsroni, "Particles-turbulence interaction," Int. J. Multiphase Flow **15**(5), 735–746 (1989).

[10] T. Tanaka and J. Eaton, "Classification of turbulence modification by dispersed spheres using a novel dimensionless number," Phys. Rev. Lett. **101**, 114502 (2008).

[11] T. Burton and J. Eaton, "Fully resolved simulations of particle-turbulence interaction," J. Fluid Mech. **545**, 67–111 (2005).

[12] T. Tanaka and J. K. Eaton, "Sub-Kolmogorov resolution particle image velocimetry measurements of particle-laden forced turbulence," J. Fluid Mech. **643**, 177–206 (2010).

[13] D. Rouson and J. Eaton, "On the preferential concentration of solid particles in turbulent channel flow," J. Fluid Mech. **428**, 149–169 (2001).

[14] K. Kiger and C. Pan, "Suspension and turbulence modification effects of solid particulates on a horizontal turbulent channel flow," J. Turbul. **3**, N19 (2002).

[15] A. Soldati and C. Marchioli, "Physics and modelling of turbulent particle deposition and entrainment: Review of a systematic study," Int. J. Multiphase Flow **35**(9), 827–839 (2009).

[16] Y. Pan and S. Banerjee, "Numerical simulation of particle interactions with wall turbulence," Phys. Fluids **8**(10), 2733–2755 (1996).

[17] Y. Li, B. McLaughlin, K. Kontomaris, and L. Portela, "Numerical simulation of particle-laden turbulent channel flow," Phys. Fluids **13**(10), 2957–2967 (2001).

[18] Y. Mito and T. Hanratty, "Effect of feedback and inter-particle collisions in an idealized gas-liquid annular flow," Int. J. Multiphase Flow **32**, 692–716 (2006).

[19] L. Zhao, H. Andersson, and J. Gillissen, "Turbulence modulation and drag reduction by spherical particles," Phys. Fluids **22**, 081702 (2010).

[20] C. Dritselis and N. Vlachos, "Numerical study of educed coherent structures in the near-wall region of a particle-laden channel flow," Phys. Fluids **20**, 055103 (2008).

[21] C. Dritselis and N. Vlachos, "Numerical investigation of momentum exchange between particles and coherent structures in low Re tubulent channel flow," Phys. Fluids **23**, 025103 (2011).

[22] J. Eaton, "Two-way coupled turbulence simulations of gas-particle flows using point-particle tracking," Int. J. Multiphase Flow **35**, 792–800 (2009).

[23] X. Shao, T. Wu, and Z. Yu, "Fully resolved numerical simulation of particle-laden turbulent flow in a horizontal channel at a low Reynolds number," J. Fluid Mech. **693**, 319–344 (2012).

[24] H. Gao, H. Li, and L.-P. Wang, "Lattice Boltzmann simulation of turbulent flow laden with finite-size particles," Comput. Math. Appl. **65**(2), 194–210 (2013).

[25] F. Lucci, A. Ferrante, and S. Elghobashi, "Is Stokes number an appropriate indicator for turbulence modulation by particles of Taylor-length-scale size?," Phys. Fluids **23**, 025101 (2011).

[26] D. H. Richter and P. P. Sullivan, "Sea surface drag and the role of spray," Geophys. Res. Lett. **40**, 656–660, doi:10.1002/grl.50163 (2013).

[27] V. N. Kudryavtsev and V. Makin, "The impact of air-flow separation on the drag of the sea surface," Boundary-Layer Meteorol. **98**, 155–171 (2001).

[28] M. R. Maxey and J. J. Riley, "Equation of motion for a small rigid sphere in nonuniform flow," Phys. Fluids **26**(4), 883–889 (1983).

[29] R. Clift, J. R. Grace, and M. E. Weber, *Bubbles, Drops, and Particles* (Academic Press, 1978).

[30] M. Boivin, O. Simonin, and K. D. Squires, "Direct numerical simulation of turbulence modulation by particles in isotropic turbulence," J. Fluid Mech. **375**, 235–263 (1998).

[31] M. Lee and J. Kim, "The structure of turbulence in a simulated plane Couette flow," in *Eighth Symposium on Turbulent Shear Flows* (Springer-Verlag, 1991), pp. 5.3.1–5.3.6.

[32] J. Komminaho, A. Lundbladh, and A. V. Johansson, "Very large structures in plane turbulent Couette flow," J. Fluid Mech. **320**, 259–285 (1996).

[33] T. Tsukahara, H. Kawamura, and K. Shingai, "DNS of turbulent Couette flow with emphasis on the large-scale structure in the core region," J. Turbul. **7**(19), N19 (2006).

[34] P. Moin and K. Mahesh, "Direct numerical simulation: A tool in turbulence research," Ann. Rev. Fluid Mech. **30**, 539–578 (1998).

[35] P. P. Sullivan and E. G. Patton, "The effect of mesh resolution on convective boundary layer statistics and structures generated by large-eddy simulation," J. Atmos. Sci. **68**, 2395–2415 (2011).

[36] P. R. Spalart, R. D. Moser, and M. M. Rogers, "Spectral methods for the Navier-Stokes equations with one infinite and two periodic directions," J. Comput. Phys. **96**, 297–324 (1991).

[37] P. P. Sullivan, J. McWilliams, and C.-H. Moeng, "Simulation of turbulent flow over idealized water waves," J. Fluid Mech. **404**, 47–85 (2000).

[38] O. Kitoh, K. Nakabyashi, and F. Nishimura, "Experimental study on mean velocity and turbulence characteristics of plane Couette flow: Low-Reynolds-number effects and large longitudinal structure," J. Fluid Mech. **539**, 199–227 (2005).

[39] C. Marchioli, A. Soldati, J. G. M. Kuerten, B. Arcen, A. Taniere, G. Goldensoph, K. D. Squires, M. F. Cargnelutti, and L. M. Portela, "Statistics of particle dispersion in direct numerical simulations of wall-bounded turbulence: Results of an international collaborative benchmark test," Int. J. Multiphase Flow **34**(9), 879–893 (2008).

[40] B. P. K. Yung, H. Merry, and T. R. Bott, "The role of turbulent bursts in particle re-entrainment in aqueous systems," Chem. Eng. Sci. **44**(4), 873–882 (1989).

[41] J. Fessler, J. Kulick, and J. Eaton, "Preferential concentration of heavy particles in a turbulent channel flow," Phys. Fluids **6**(11), 3742–3749 (1994).

[42] J. Kulick, J. Fessler, and J. Eaton, "Particle response and turbulence modification in fully developed channel flow," J. Fluid Mech. **277**, 109–134 (1994).

[43] M. Righetti and G. Romano, "Particle-fluid interactions in a plane near-wall turbulent flow," J. Fluid Mech. **505**, 93–121 (2004).

[44] R. Sureshkumar, A. Beris, and R. Handler, "Direct numerical simulation of the turbulent channel flow of a polymer solution," Phys. Fluids **9**(3), 743–755 (1997).

[45] C. Rogers and J. Eaton, "Effect of small particles on fluid turbulence in a flat-plate, turbulent boundary layer in air," Phys. Fluids A: Fluid Dyn. **3**(5), 928–937 (1991).

[46] Y. Tsuji, Y. Morikawa, and H. Shiomi, "LDV measurements of an air-solid two-phase flow in a vertical pipe," J. Fluid Mech. **139**, 417–434 (1984).

[47] C. Poelma and G. Ooms, "Particle-turbulence interaction in a homogeneous, isotropic turbulent suspension," Appl. Mech. Rev. **59**(2), 78–90 (2006).

[48] J. Bec, L. Biferale, M. Cencini, A. Lanotte, S. Musacchio, and F. Toschi, "Heavy particle concentration in turbulence at dissipative and inertial scales," Phys. Rev. Lett. **98**, 084502 (2007).

[49] G. Falkovich, A. Fouxon, and M. Stepanov, in *Sediment and Sediment Transport*, edited by A. Gyr and W. Kinzelbach (Kluwer Academic Publishers, Dordrecht, 2003), pp. 155–158.

[50] W. Willmarth and S. Lu, "Structure of the Reynolds stress near the wall," J. Fluid Mech. **55**, 65–92 (1972).

[51] R. Adrian, "Hairpin vortex organization in wall turbulence," Phys. Fluids **19**(4), 041301 (2007).

[52] J. Zhou, R. Adrian, S. Balachandar, and T. M. Kendall, "Mechanisms for generating coherent packets of hairpin vortices in channel flow," J. Fluid Mech. **387**, 353–396 (1999).

[53] M. Rashidi, G. Hetsroni, and S. Banerjee, "Particle-turbulence interaction in a boundary layer," Int. J. Multiphase Flow **16**(6), 935–949 (1990).

[54] O. Druzhinin, "On the two-way interaction in two-dimensional particle-laden flows: The accumulation of particles and flow modification," J. Fluid Mech. **297**, 49–76 (1995).